



<b>Publication Year</b>	2021
<b>Acceptance in OA</b>	2022-04-01T10:53:48Z
<b>Title</b>	Into the storm: diving into the winds of the ultra-hot Jupiter WASP-76 b with HARPS and ESPRESSO
<b>Authors</b>	Seidel, J. V., Ehrenreich, D., Allart, R., Hoeijmakers, H. J., Lovis, C., Bourrier, V., Pino, Lorenzo, Wyttenbach, A., Adibekyan, V., Alibert, Y., BORSA, Francesco, Casasayas-Barris, N., CRISTIANI, Stefano, Demangeon, O. D. S., DI MARCANTONIO, Paolo, Figueira, P., González Hernández, J. I., Lillo-Box, J., Martins, C. J. A. P., Mehner, A., MOLARO, Paolo, Nunes, N. J., Palle, E., Pepe, F., Santos, N. C., Sousa, S. G., SOZZETTI, Alessandro, Taberner, H. M., Zapatero Osorio, M. R.
<b>Publisher's version (DOI)</b>	10.1051/0004-6361/202140569
<b>Handle</b>	<a href="http://hdl.handle.net/20.500.12386/32077">http://hdl.handle.net/20.500.12386/32077</a>
<b>Journal</b>	ASTRONOMY & ASTROPHYSICS
<b>Volume</b>	653

# Into the storm: diving into the winds of the ultra-hot Jupiter WASP-76 b with HARPS and ESPRESSO

J. V. Seidel<sup>1</sup> , D. Ehrenreich<sup>1</sup>, R. Allart<sup>2,1</sup> , H. J. Hoeijmakers<sup>3</sup> , C. Lovis<sup>1</sup>, V. Bourrier<sup>1</sup>, L. Pino<sup>4</sup>, A. Wyttenbach<sup>5</sup>,  
V. Adibekyan<sup>6,7</sup>, Y. Alibert<sup>8</sup>, F. Borsa<sup>9</sup>, N. Casasayas-Barris<sup>13,19,20</sup>, S. Cristiani<sup>11</sup>, O. D. S. Demangeon<sup>6,7</sup>,  
P. Di Marcantonio<sup>10</sup>, P. Figueira<sup>12,6</sup>, J. I. González Hernández<sup>13</sup>, J. Lillo-Box<sup>10</sup>, C. J. A. P. Martins<sup>6,14</sup>,  
A. Mehner<sup>12</sup>, P. Molaro<sup>11,18</sup>, N. J. Nunes<sup>15</sup>, E. Palle<sup>13,19</sup>, F. Pepe<sup>1</sup>, N. C. Santos<sup>6,7</sup>, S. G. Sousa<sup>6</sup>, A. Sozzetti<sup>16</sup>,  
H. M. Taberner<sup>6,17</sup>, and M. R. Zapatero Osorio<sup>17</sup>

<sup>1</sup> Observatoire astronomique de l'Université de Genève, Chemin Pegasi 51b, 1290 Versoix, Switzerland  
e-mail: [julia.seidel@unige.ch](mailto:julia.seidel@unige.ch)

<sup>2</sup> Department of Physics, and Institute for Research on Exoplanets, Université de Montréal, Montréal, H3T 1J4, Canada

<sup>3</sup> Lund Observatory, Box 43, Sölvegatan 27, 22100 Lund, Sweden

<sup>4</sup> INAF – Osservatorio Astrofisico di Arcetri, Largo E. Fermi 5, 50125 Florence, Italy

<sup>5</sup> Université Grenoble Alpes, CNRS, IPAG, 38000 Grenoble, France

<sup>6</sup> Instituto de Astrofísica e Ciências do Espaço, CAUP, Universidade do Porto, Rua das Estrelas, 4150-762 Porto, Portugal

<sup>7</sup> Departamento de Física e Astronomia, Faculdade de Ciências, Universidade do Porto, Rua do Campo Alegre, 4169-007 Porto, Portugal

<sup>8</sup> Physikalisches Institut & NCCR PlanetS, Universität Bern, 3012 Bern, Switzerland

<sup>9</sup> INAF – Osservatorio Astronomico di Brera, Via E. Bianchi 46, 23807 Merate (LC), Italy

<sup>10</sup> Centro de Astrobiología (CAB, CSIC-INTA), Departamento de Astrofísica, ESAC campus 28692 Villanueva de la Cañada, Madrid, Spain

<sup>11</sup> INAF – Osservatorio Astronomico di Trieste, via Tiepolo 11, 34143 Trieste, Italy

<sup>12</sup> European Southern Observatory (ESO) – Alonso de Cordova 3107, Vitacura, Santiago, Chile

<sup>13</sup> Instituto de Astrofísica de Canarias, Via Lactea sn, 38200, La Laguna, Tenerife, Spain

<sup>14</sup> Centro de Astrofísica, Universidade do Porto, Rua das Estrelas, 4150-762 Porto, Portugal

<sup>15</sup> Instituto de Astrofísica e Ciências do Espaço, Faculdade de Ciências da Universidade de Lisboa, Campo Grande, 1749-016 Lisboa, Portugal

<sup>16</sup> INAF – Osservatorio Astrofisico di Torino, Strada Osservatorio, 20 10025 Pino Torinese (TO), Italy

<sup>17</sup> Centro de Astrobiología (CSIC-INTA), Ctra. de Ajalvir km 4, 28850, Torrejón de Ardoz, Madrid, Spain

<sup>18</sup> Institute for Fundamental Physics (IFPU), Via Beirut 2, 34151 Grignano TS, Italy

<sup>19</sup> Departamento de Astrofísica, Universidad de La Laguna, 38200 San Cristobal de La Laguna, Spain

<sup>20</sup> Leiden Observatory, Leiden University, Postbus 9513, 2300 RA Leiden, The Netherlands

Received 15 February 2021 / Accepted 20 July 2021

## ABSTRACT

**Context.** Despite swift progress in the characterisation of exoplanet atmospheres in composition and structure, the study of atmospheric dynamics has not progressed at the same speed. While theoretical models have been developed to describe the lower layers of the atmosphere, and independently, the exosphere, little is known about the intermediate layers up to the thermosphere.

**Aims.** We aim to provide a clearer picture of atmospheric dynamics for the class of ultra-hot Jupiters, which are highly irradiated gas giants, based on the example of WASP-76 b.

**Methods.** We jointly analysed two datasets that were obtained with the HARPS and ESPRESSO spectrographs to interpret the resolved planetary sodium doublet. We then applied the MERC code, which retrieves wind patterns, speeds, and temperature profiles on the line shape of the sodium doublet. An updated version of MERC, with added planetary rotation, also provides the possibility of modelling the latitude dependence of the wind patterns.

**Results.** We retrieve the highest Bayesian evidence for an isothermal atmosphere, interpreted as a mean temperature of  $3389 \pm 227$  K, a uniform day- to nightside wind of  $5.5^{+1.4}_{-2.0}$  km s<sup>-1</sup> in the lower atmosphere with a vertical wind in the upper atmosphere of  $22.7^{+4.9}_{-4.1}$  km s<sup>-1</sup>, switching atmospheric wind patterns at 10<sup>-3</sup> bar above the reference surface pressure (10 bar).

**Conclusions.** Our results for WASP-76 b are compatible with previous studies of the lower atmospheric dynamics of WASP-76 b and other ultra-hot Jupiters. They highlight the need for vertical winds in the intermediate atmosphere above the layers probed by global circulation model studies to explain the line broadening of the sodium doublet in this planet. This work demonstrates the capability of exploiting the resolved spectral line shapes to observationally constrain possible wind patterns in exoplanet atmospheres. This is an invaluable input to more sophisticated 3D atmospheric models in the future.

**Key words.** planets and satellites: atmospheres – planets and satellites: individual: WASP-76 b – techniques: spectroscopic – line: profiles – methods: data analysis

## 1. Introduction

The study of hot Jupiters is revealing a more and more detailed picture of their atmospheric composition. Through transmission spectroscopy, the existence of a wide range of atoms, ions, and molecules in hot Jupiter atmospheres has been inferred (e.g. [Evans et al. 2018](#); [Casasayas-Barris et al. 2019](#); [Hoeijmakers et al. 2019, 2020](#); [Tabernero et al. 2021](#)), and established results were revised with higher resolution ([Casasayas-Barris et al. 2021](#)). We can also detect clouds and hazes (e.g. [Powell et al. 2019](#); [Parmentier et al. 2021](#); [Gao et al. 2020](#); [Barstow 2020](#); [Allart et al. 2020](#)), the thermal structure of the atmosphere (e.g. [Line et al. 2016](#); [Evans et al. 2018](#); [Gibson et al. 2020](#); [Yan et al. 2020](#); [Baxter et al. 2020](#)), even chemical abundances of the detected elements (e.g. [Line et al. 2014](#); [Brogi & Line 2019](#); [Pino et al. 2020](#)), and condensation of iron ([Ehrenreich et al. 2020](#); [Borsa et al. 2021](#)).

The first attempt of directly measuring atmospheric winds based on prior theoretical work ([Knutson et al. 2008](#)) was performed with the CO band of HD 209458 b. It found a blueshift of  $2 \text{ km s}^{-1}$  compared to the systemic velocity, indicating a day-to nightside wind ([Snellen et al. 2010](#)). Similarly, studying the bands of CO and H<sub>2</sub>O in the exoplanet  $\beta$  Pic b, [Snellen et al. \(2014\)](#) found a rotational velocity of  $v_{\text{rot}} = 25 \pm 3 \text{ km s}^{-1}$ . The conceptual proof of this technique started further studies that constrained the rotational speed in the lower atmosphere of hot Jupiters, most of them consistent with the tidally locked nature of these planets ([Louden & Wheatley 2015](#); [Brogi et al. 2016](#)).

The sodium doublet is especially well suited to bridge the missing pressure regions between the lower atmosphere that is probed with molecular bands and the exosphere. It is a resonant doublet and probes the terminator up until the thermosphere in high resolution ([Wytenbach et al. 2015](#)). Based on this result, the survey called Hot Exoplanet Atmospheres Resolved with Transmission Spectroscopy (HEARTS) was created and has provided a number of interesting datasets for the study of atmospheric winds in high resolution ([Wytenbach et al. 2017](#); [Seidel et al. 2019, 2020a,c](#); [Hoeijmakers et al. 2020](#)). With the possibility of resolving the line shape of single spectral lines from high-resolution transmission spectra, vertical layers below the thermosphere have become accessible through the sodium doublet and similar lines. For example, the Balmer lines have recently been used by [Wytenbach et al. \(2020\)](#) to study Parker winds and rotational broadening in the ultra-hot Jupiter KELT-9 b and by [Cauley et al. \(2021\)](#) to study the rotational velocity of the ultra-hot Jupiter WASP-33 b. While [Wytenbach et al. \(2020\)](#) reported zonal wind speeds consistent with planetary rotation for KELT-9 b, [Cauley et al. \(2021\)](#) reported evidence of high zonal wind speeds across the terminator and tentative evidence of a day- to nightside wind. [Seidel et al. \(2020b\)](#) combined a nested sampling algorithm with a forward model of different wind patterns to retrieve the line shape of the sodium doublet for HD 189733 b, thus exploring the full parameter space created by the wind speed, direction, temperature, and continuum level. The retrieval revealed a high velocity of an outwards expanding wind in the intermediate layers of the atmosphere that drives the atmospheric mass-loss in the exosphere.

Probing the lower atmosphere using the iron signature in WASP-76 b, [Ehrenreich et al. \(2020\)](#) measured a combination of planetary rotation and day- to nightside winds with ESPRESSO<sup>1</sup>. Revisiting the data on WASP-76 b taken with

HARPS<sup>2</sup>, [Kesseli & Snellen \(2021\)](#) were able to confirm the results with the same technique even on the less precise HARPS data, opening up an avenue to revisit HARPS data for a multitude of similar exoplanets. The sodium doublet of WASP-76 b, first detected by [Seidel et al. \(2019\)](#), was recently observed with ESPRESSO, which provided an unparalleled precision of the line shape with a single transit ([Tabernero et al. 2021](#)). Based on this work, we study the atmospheric winds in WASP-76 b through the sodium doublet, probing the atmosphere up to the thermosphere, with the MERC retrieval code ([Seidel et al. 2020b](#)).

## 2. WASP-76 b datasets

We used two different datasets for WASP-76 b in this study, taken with the HARPS and ESPRESSO spectrographs. The HARPS WASP-76 b sodium doublet data published in [Seidel et al. \(2019\)](#) are based on three transits taken as part of the HEARTS survey (ESO program 100.C-0750; PI: Ehrenreich). However, since then, the system parameters for WASP-76 were updated. We address the impact of these changes in the following section.

### 2.1. Revised system parameters and effect on the HARPS dataset

Since the analysis of the sodium doublet from the HARPS data for WASP-76 b ([Seidel et al. 2019](#)), a close companion to the host star was detected by [Bohn et al. \(2020\)](#) with a separation of  $0.436 \pm 0.003 \text{ arcsec}$  and a K-band magnitude difference of  $2.30 \pm 0.05$ . In consequence, the planetary parameters were updated in [Southworth et al. \(2020\)](#) and [Ehrenreich et al. \(2020\)](#). This analysis uses the new parameters from Table 1 with the stellar companion, instead of the values used by [Seidel et al. \(2019\)](#) from the discovery paper of [West et al. \(2016\)](#). The change in parameters can affect the relative velocities of the system, the star, and the planet and thus lead to a different line shape. We subsequently decided to re-analyse the HARPS dataset. The two velocities used in building the transmission spectrum that can affect the line shape are the semi-amplitude of the stellar radial velocities (RVs),  $K_*$ , and the systemic velocity,  $v_{\text{sys}}$ , which are both taken from [Ehrenreich et al. \(2020\)](#), see Table 1. The parameters were verified in [Tabernero et al. \(2021\)](#), who created a 2D map of the sodium detection for the dataset we used here, which clearly shows the planet trace in the stellar rest frame ([Tabernero et al. 2021](#), Fig. 5). An analysis of the effect of the planetary orbital velocity on the results we present is provided in Appendix B, which shows that the broadening of the lines cannot stem from imprecise values of the orbital parameters.

We reduced the data in the same way as [Seidel et al. \(2019\)](#), but with the updated system parameters. We used the 2D echelle spectral images produced by the HARPS Data Reduction Pipeline (DRS v3.5) and discarded 15 exposures in night 3 that were affected by cirrus clouds, just as in [Seidel et al. \(2019\)](#). We then applied `molecfit` ([Smette et al. 2015](#); [Kausch et al. 2015](#); [Allart et al. 2017](#)) to correct for tellurics and shifted all spectra to the stellar rest frame. We combined all out-of-transit spectra to the normalised master-out and extracted the planetary signal by dividing each in-transit spectrum with the master-out. Lastly, we created the transmission spectrum by shifting the in-transit spectra into the planetary rest frame and summed over them for a sufficient signal-to-noise ratio (S/N) to detect the sodium feature. Figure 1 shows the comparison between the spectrum as presented in [Seidel et al. \(2019\)](#) and the new analysis with the updated parameters. The difference between the two datasets

<sup>1</sup> Echelle SPectrograph for Rocky Exoplanets and Stable Spectroscopic Observations.

<sup>2</sup> High Accuracy Radial velocity Planet Searcher.

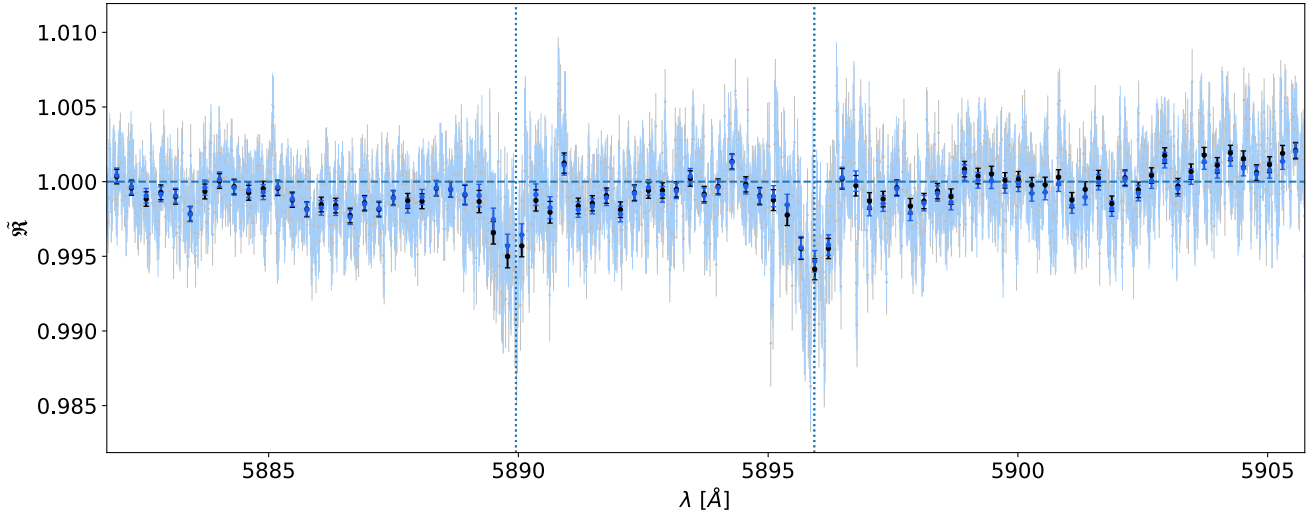


**Fig. 1.** HARPS datasets before and after the system parameter update normalised to 1. In black we show the HARPS dataset as published in Seidel et al. (2019), and in blue, we show the re-analysed dataset with the new system parameters. The vertical dashed blue lines indicate the line centre of the sodium doublet lines.

**Table 1.** Planetary and stellar parameters.

Taken from Ehrenreich et al. (2020):	
Planetary radius, $R_p$ [ $R_J$ ]	$1.854^{+0.077}_{-0.076}$
Planetary mass, $M_p$ [ $M_J$ ]	$0.894^{+0.014}_{-0.013}$
Stellar radius, $R_*$ [ $R_\odot$ ]	$1.756 \pm 0.071$
Stellar mass, $M_*$ [ $M_\odot$ ]	$1.458 \pm 0.021$
Orbital semi-major axis, $a$ [au]	$0.0330 \pm 0.0002$
Scaled $a$ , $a/R_*$	$4.08^{+0.06}_{-0.02}$
Inclination [deg]	$89.623^{+0.005}_{-0.034}$
Eccentricity, $e$ (fixed)	0.0
Transit depth, $\Delta T$	$0.01178^{+0.00077}_{-0.00076}$
$K_\star$ [ $\text{m s}^{-1}$ ]	$116.02^{+1.29}_{-1.35}$
$v_{\text{sys}}$ [ $\text{km s}^{-1}$ ]	$-1.11 \pm 0.50$
Mid-transit time, [BJD] - 2 450 000	$8080.626165^{+0.000418}_{-0.000367}$
Transit duration [d]	0.15972
Ingress duration [d]	0.01639
Period [d]	$1.80988198^{+0.00000064}_{-0.00000056}$
Impact parameter	$0.027^{+0.13}_{-0.023}$
$T_{\text{eq}}$ [K]	$2228 \pm 122$

is mainly driven by the updated values for the radii. The new dataset is also shown in the upper panel of Fig. 2. While the changes are less than 1% compared to the spectrum published by Seidel et al. (2019), both lines of the sodium doublet are fainter and narrower than before. This justifies the new reduction of the data with regard to the aim of this work: to extract information from the sodium doublet line shape. However, the effect of the updated system parameters does not change any of the conclusions drawn in Seidel et al. (2019).

## 2.2. ESPRESSO dataset

The transmission spectrum of WASP-76 b around the sodium doublet was created from observations with the ESPRESSO spectrograph at the ESO VLT telescope in Paranal, Chile

(Pepe et al. 2021). The observations were performed as part of ESO program 1102.C-0744 (ESPRESSO GTO, Ehrenreich et al. 2020; Tabernero et al. 2021). Two transits of WASP-76 b were recorded, on 3 September 2018 (night one) and 31 October 2018 (night two). For an overview of observational conditions, see Tabernero et al. (2021). In night 1, four spectra were removed due to high airmass<sup>3</sup>, and in night 2, three spectra were discarded likewise.

To have planetary spectra that were obtained with the same technique (thus minimising the systematics that different methods of spectrum extraction might introduce in our analysis), we re-reduced the ESPRESSO data. The trace of the stellar sodium line centre was masked to eliminate residuals in all spectra with a window of  $\pm 4 \text{ km s}^{-1}$ . Each remaining spectrum was corrected for cosmics and the transmission spectrum built following Seidel et al. (2019, 2020a). We applied molecfit (Smette et al. 2015; Kausch et al. 2015; Allart et al. 2017) to correct both nights for the effect of telluric lines and used the SKYSUB S2D output files of the DRS pipeline, which are corrected for the effect of sky emission and blaze corrected. We corrected the telluric lines down to the noise level for all airmasses and verified that no residuals are visible in the combined master spectrum. As shown by Seidel et al. (2019) for the HARPS data and by Tabernero et al. (2021) for the ESPRESSO data, the Rossiter-McLaughlin (RM) effect and centre-to-limb effects induce variations in the transmission spectra at the level of 0.04%, which is lower than the combined error on our final dataset  $\pm 0.1\%$ . Two possible techniques to correct for the RM effect, a numerical approximation (Wytenbach et al. 2020) or modelling (e.g. Casasayas-Barris et al. 2019) were compared by Seidel et al. (2020b) for the hot Jupiter HD 189733 b and showed differences of approximately 0.1%, highlighting that the selection of different correction techniques introduces different systematic errors on the line shape. As shown by Casasayas-Barris et al. (2021), the RM correction also depends on the synthetic stellar spectra, and more work is needed to properly establish which model spectra should be used for RM corrections. However, for the ESPRESSO dataset, which is more sensitive to the RM effect, we masked the trace of the

<sup>3</sup> airmass < 2.0, for consistency with HARPS analysis, ESPRESSO ADC restrictions at 2.2.

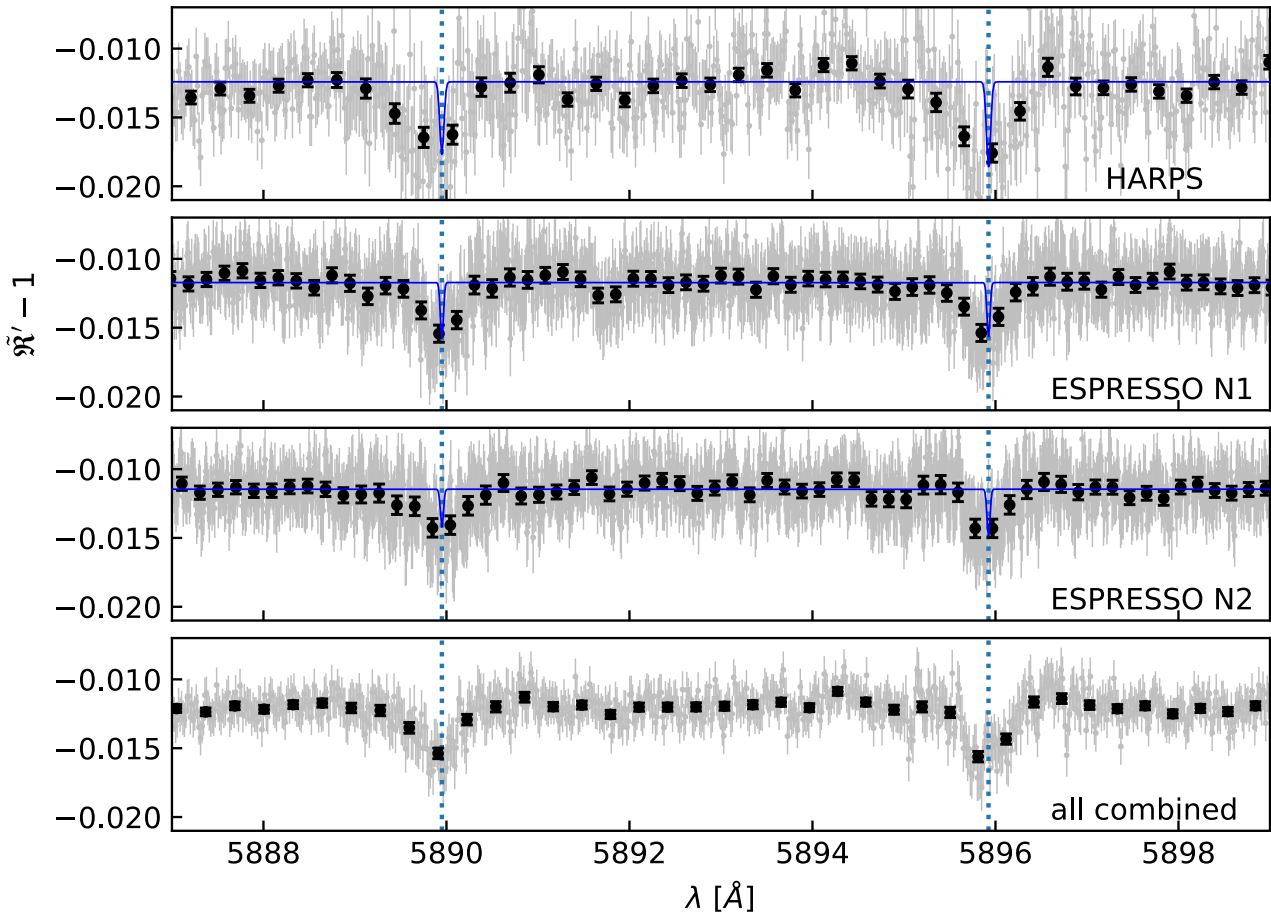


**Fig. 2.** Overview of the sodium doublet transmission spectra used in this work, normalised to 0 with the added contribution of the obscure disk of the planet. The disk contribution depends on the white-light radius and is therefore only a best-effort approximation for the real continuum in the order of the sodium doublet. Because the same radius is also used for the retrieval, this has no effect on our conclusions. *Top panel:* HARPS spectrum from Seidel et al. (2019) reprocessed with the updated system parameters. *Centre panels:* ESPRESSO spectrum for each night. *Bottom panel:* all three datasets combined. The line centres of the sodium lines are indicated as dashed vertical blue lines, and the line spread function of the respective instrument is shown as a blue graph.

stellar sodium line centre, which coincides with the area of maximum impact from the RM effect. In conclusion, for the particular dataset presented here, a correction of the RM effect would introduce a larger uncertainty on our dataset, and we opted not to correct for this effect in the following, but to minimise it through masking.

Because of interference patterns created by Coudé train optics in ESPRESSO, the combined transmission spectrum shows sinusoidal noise (wiggles) instead of a straight base line (Allart et al. 2020; Tabernero et al. 2021). A sinusoidal fit was performed on the final transmission spectrum for each night to correct for this feature. We combined both nights and both orders containing the sodium doublet (116 and 117) and show the resulting final transmission spectrum in the middle panel of Fig. 2. The independent re-analysis of the ESPRESSO transmission spectrum is compatible with the spectrum presented in Tabernero et al. (2021).

### 2.3. Combined dataset and compatibility

The combined HARPS dataset and the ESPRESSO datasets for both nights can be found in Fig. 2. ESPRESSO has a higher throughput and is installed on a larger telescope than HARPS. Depending on the sky conditions, it is therefore expected that

three to four HARPS transits, as in our HARPS dataset, are equivalent to one ESPRESSO transit. While the line shapes are roughly reproduced in all three datasets, the datasets show a difference in line depth. As already analysed by Seidel et al. (2019) for the HARPS dataset, the three combined HARPS nights were affected by thin cloud cover and thus varying line depths that had to be corrected for. While the line depths within the HARPS dataset were subsequently compatible, the uncertainty of HARPS is comparatively large. The two nights of ESPRESSO data re-analysed here were first studied by Tabernero et al. (2021), who found an average line depth of  $0.417 \pm 0.035\%$  in night 1 and  $0.270 \pm 0.028\%$  in night 2 (see overview in Table 2). In consequence, the three datasets show no visible variation in line shape when rescaled beyond what is expected from uncertainties, but they differ in line depth. Stellar activity was monitored for the HARPS dataset with simultaneous photometric observations (Seidel et al. 2019) and for the ESPRESSO dataset through the Ca II H and K lines, again showing no stellar activity that could account for the differing line depths. Alternatively, the difference could stem from a change in mean atmospheric temperature between the nights and thus a change in transit depth. Therefore the value retrieved for the mean temperature of the atmosphere should be seen as a mean value and upper boundary for the real temperature of the atmosphere

**Table 2.** Relative absorption depth atmospheric sodium, both lines combined.

Dataset	abs. depth (%)	Reference
HARPS N1	$0.419 \pm 0.078$	Seidel et al. (2019)
HARPS N2	$0.361 \pm 0.060$	Seidel et al. (2019)
HARPS N3	$0.362 \pm 0.045$	Seidel et al. (2019)
HARPS combined	$0.381 \pm 0.036$	
ESPRESSO N1	$0.417 \pm 0.035$	Taberner et al. (2021)
ESPRESSO N2	$0.270 \pm 0.028$	Taberner et al. (2021)

(see Sect. 4). Additionally, to reduce the effect of temporal temperature variations, the three datasets were combined to obtain a more precise dataset.

Because the doublet lines are much broader than the line spread functions of the instruments in question (12, 11, and 13 times wider from top to bottom in Fig. 2), we can re-bin the ESPRESSO data ( $R \sim 138\,000$ ) on the lower-resolution HARPS wavelength grid ( $R \sim 115\,000$ ) and combine the three datasets of similar resolution (combined HARPS data, and ESPRESSO nights 1 and 2). We weighted each dataset with the respective mean S/N over the order of the sodium doublet: 48.58, 61.20, and 53.39, corresponding to a fraction of 29.77, 37.51, and 32.72% in the combined transmission spectrum. The resulting combined transmission spectrum of the sodium doublet, which is comprised of the three equivalent datasets and used in the rest of this work, is shown in the lower panel of Fig. 2.

A possible caveat for the study of line shapes is Doppler-smearing, which is introduced by the continuous change of the orbital velocity of the planet during one exposure (Ridden-Harper et al. 2016; Wyttenbach et al. 2020; Cauley et al. 2021) and the line spread function of the instrument. The exposure times for the HARPS datasets and ESPRESSO night 2 were 300 s on average, and for ESPRESSO night 1, the exposure time was 600 s. The instrument and telescope overheads, and thus the time between exposures, is 32 s for HARPS and 68 s for ESPRESSO. We estimate the maximum Doppler-smear of the planet orbital velocity from the exposure times at  $2.4 \text{ km s}^{-1}$  for the HARPS and night 2 ESPRESSO dataset, and  $4.7 \text{ km s}^{-1}$  for the night 1 ESPRESSO dataset. This means that the mean smear over the entire exposure is approximately one resolution element and affects the data for this particular system little, but we address the additional uncertainty in the discussion. MERC directly accounts for the instrument resolution.

### 3. Updates to MERC

MERC (Seidel et al. 2020b) combines a nested-sampling retrieval algorithm with a forward model to produce theoretical line profiles and then compare them with the provided dataset. The forward model includes Doppler-broadening by a variety of global wind patterns, which are described below. The algorithm provides the Bayesian evidence  $|\ln \mathcal{Z}|$  for each forward model and the median of the marginalised posterior distributions of the parameters, the best-fit parameters, within the set parameter space. The difference in Bayesian evidence  $|\ln \mathcal{B}_{01}|$  then ranks the models between each other and shows the significance of the selection of one model over another through the Jeffrey scale (see Table 3 or Trotta 2008 and Skilling 2006). Table 3 together with a more in-depth explanation can also be found in Lavie et al.

**Table 3.** Empirical scale to judge the evidence when comparing two models  $M_0$  and  $M_1$ , called a ‘Jeffrey scale’.

$ \ln \mathcal{B}_{01} $	Odds	Probability	Strength of evidence
$<1.0$	$<3 : 1$	$<0.750$	Inconclusive
1.0	$\sim 3 : 1$	0.750	Weak evidence
2.5	$\sim 12 : 1$	0.923	Moderate evidence
5.0	$\sim 150 : 1$	0.993	Strong evidence

(2017) or Seidel et al. (2020b). Further details on MERC can be found in Seidel et al. (2020b).

#### 3.1. Wind patterns

MERC can model different wind patterns impacting the spectral line shape and offset: a day- to nightside wind, a super-rotational wind, and a vertical wind, as well as a combination of the first two patterns in the lower atmosphere and a vertical wind in the upper atmosphere.

To implement these wind patterns in the line of sight (LOS), we calculated the wind broadening for one atmospheric slice in the LOS (see Seidel et al. 2020b for details or Fig. 3 for an illustration). The atmospheric slice was divided into cells, and each atmospheric profile in the respective cells was Doppler-shifted by the corresponding wind velocity component in the LOS. Summing over the cells to create the slice then led to an overall Doppler broadening. For a full 3D treatment of the atmospheric dynamics, this procedure would have to be repeated for each cell through which the light passes, which requires computing times incompatible with a nested-sampling retrieval approach. Therefore Seidel et al. (2020b) used the symmetry of the proposed wind patterns and rotated the atmospheric slice by  $2\pi$  or a fraction thereof to obtain the full atmosphere. While preferable for computational reasons, this approach restricts the wind patterns to constant wind speeds in latitude throughout the planet atmosphere. Additionally, co-rotation of the atmosphere with the planet rotation cannot be accounted for because it depends on latitude. Especially for a super-rotational or day- to nightside wind, work with global circulation models (GCMs) has shown that they have a more jet-like structure for hot Jupiters, with stronger winds at the equator than at the poles (e.g. Showman et al. 2009).

Subsequently, we updated MERC and introduced the possibility for a solid-body-like latitude dependence of the super-rotational or day- to nightside wind speeds, as was implemented for Parker winds and rotation in Wyttenbach et al. (2020). The vertical wind only expands the atmosphere, regardless of the latitude. This approach produces the strongest wind at the equator and imposes a reduction of zonal winds to zero at the poles. The new calculation of the wind speed in the LOS, compared to Eq. (7) from Seidel et al. (2020b), is then

$$|v|_{\text{LOS}} = \pm |v_{\text{srot/dtn}}| \cdot \frac{R_p + b}{\sqrt{(R_p + b)^2 + x^2}} \cdot \cos \theta, \quad (1)$$

where  $\theta$  is the angle between the equator and the radial vector to the current cell (an approximation of its latitude),  $R_p$  is the planet white-light radius,  $b$  is the impact factor (the current position above the surface in  $z$ , see Fig. 2 in Seidel et al. (2020b) for a visualisation), and  $x$  is the current position of the cell along the LOS, expressing the position of the cell in Cartesian coordinates. In this treatment of atmospheric slices, the zonal winds are not

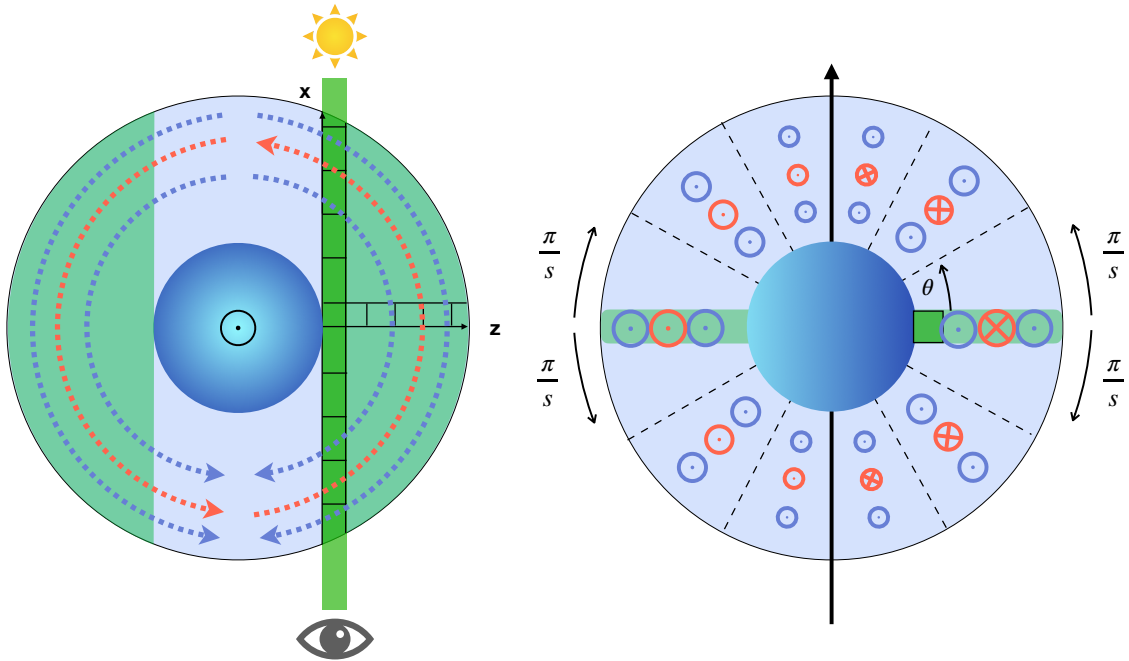


**Fig. 3.** Illustration of the implementation of the day- to nightside wind (updated version of Fig. 3 from Seidel et al. 2020b). All other zonal wind patterns are implemented in the same fashion. A polar view of the atmosphere is shown on the left and an equatorial view on the right. The wind direction and strength are indicated in blue, and the direction and strength of the rotational velocity of the planet is shown in red. Dashed black lines indicate the border between sectors. For illustration purposes, we set  $s = 3$ , see text. *Left:* dotted arrows indicate the direction of the velocities. The extinction coefficient is calculated in altitude along the  $z$ -axis and then transposed in the  $x$ -direction along the LOS (dark green cells). The LOS is then iterated upward in  $z$  until the top of the atmosphere is reached, and all values are saved in a 2D grid (here visualised as a slice in light green). In each bin of the 2D grid, the combined velocity of wind and planet rotation and the broadened profile are calculated and stored (see Seidel et al. 2020b for more details). *Right:* position of the observer. Points indicate a flow towards the observer, crosses indicate a flow away from the observer. The process described on the left is repeated for each sector, where the velocities are adjusted for the latitude via Eq. (1) and then rotated by  $\pi/s$  (or  $\pi/2s$ , depending on the symmetry) to create the full atmosphere. In this simplification of the atmosphere, the wind is not parallel to the equator, but points towards the anti-stellar point. This reduces calculation time significantly because it reduces the problem from 3D to 2D for each sector, with the extinction coefficient only calculated once in 1D, while providing quasi-3D insights into the wind structure.

parallel to the equator, but point towards the anti-stellar point (see Fig. 3). This geometry has no effect on the LOS component of the velocity, which drives the line broadening and is only an artefact of the chosen geometry.

The planetary rotation, assuming the planet is tidally locked, adds a velocity of

$$|v_{\text{planet,rot}}|_{\text{LOS}} = \frac{2\pi(R_p + b)}{P} \cdot \cos \theta \quad (2)$$

to each cell, with  $P$  as the rotation period. The planetary rotation is added to all models with or without winds.

The two velocity grids from the planetary rotation and the wind were co-added to obtain the LOS velocity. Because the stored atmospheric slice has to be broadened by the LOS wind speed in each cell, this computation cannot be made for each possible angle  $\theta$ . We introduced a sector variable  $s$  that slices each quarter of each hemisphere (see Fig. 3 or Wyttenbach et al. 2020) into sub-sectors. The velocities were therefore only calculated once for each sector and then rotated by  $\frac{\pi}{s}$ .  $\theta$  is defined as the angle in the centre of the sector. We tested different numbers of sectors (between 3 and 48 in steps of 3) and found changes of less than 1% in the final model spectrum for  $s \geq 9$ . In consequence, all models in this work were calculated with nine sectors. The approach of introducing latitude-dependent sectors introduces a new dimension to MERC and thus a quasi-3D

calculation of the atmosphere at the terminator probed by transmission spectroscopy. However, some assumptions were still made for the sake of reducing the computational cost: we assumed that the planet is tidally locked and that the planetary obliquity is perpendicular to the orbital plane. Both these assumptions are reasonable for exoplanets as close to their host star as WASP-76 b (West et al. 2016).

Additionally, as already mentioned in Seidel et al. (2020b), the zonal wind patterns, now including the planetary rotation, are not axisymmetric with the rotational axis of the planet, but spherically symmetric. Because we integrated over the entire terminator and are only interested in the LOS components, this has no significant effect on the resulting line profile. On a similar note, for a proper time-resolved treatment of the day- to nightside wind, we would have to take into account the orbital inclination and angle of the current position ( $\zeta$  in Fig. 3 of Ehrenreich et al. 2020) because the real symmetry axis is the connector between star and planet in a tidally locked system, and not the LOS. The  $\cos(i)$  of the orbital inclination is close to 1 and was subsequently ignored, and the orbital angle can be disregarded as well because we integrated over the entire transit, averaging at transit centre where the real symmetry axis and the LOS are parallel.

We applied the latitude-dependent wind patterns as well as the unmodulated constant wind patterns to determine whether the winds in WASP-76 b show a tendency to be restricted into zonal jets or if a more uniform wind flow along the terminator

**Table 4.** Overview of the different prior ranges of the models.

Model	$T_{\text{iso}}$ [K]	NaX	$v_{\text{srot}}$ [km s <sup>-1</sup> ]	$v_{\text{dtn}}$ [km s <sup>-1</sup> ]	$v_{\text{ver}}$ [km s <sup>-1</sup> ]
Isothermal	[1500, 4000]	[-5.0, -1.0]	–	–	–
$T$ gradient	[800, 4000],[2000, 6000] <sup>(a)</sup>	[-5.0, -1.0]	–	–	–
dtn	[1500, 4000]	[-5.0, -1.0]	–	[0.1,40.0]	–
dtn <sub>cos<math>\theta</math></sub>	[1500, 4000]	[-5.0, -1.0]	–	[0.1,40.0]	–
srot	[1500, 4000]	[-5.0, -1.0]	[0.1,40.0]	–	–
srot <sub>cos<math>\theta</math></sub>	[1500, 4000]	[-5.0, -1.0]	[0.1,40.0]	–	–
ver	[1500, 4000]	[-5.0, -1.0]	–	–	[0.1,40.0]
srot, ver	[1500, 4000]	[-5.0, -1.0]	[0.1,20.0]	–	[0.1,40.0]
dtn, ver	[1500, 4000]	[-5.0, -1.0]	–	[0.1,20.0]	[0.1,40.0]
dtn <sub>cos<math>\theta</math></sub> , ver	[1500, 4000]	[-5.0, -1.0]	–	[0.1,20.0]	[0.1,40.0]

**Notes.** <sup>(a)</sup>Bottom and top temperature for creating a temperature gradient.

is preferred. We took the planetary rotation into account for all retrievals in this work.

### 3.2. Degeneracies and the continuum

We did not modify the approach of Seidel et al. (2020b) regarding the fit to the spectral continuum, where we followed the simple description of the degeneracy between the sodium abundance and the pressure scaling as presented in Lecavelier Des Etangs et al. (2008) and Heng et al. (2015) and retrieved a degeneracy parameter NaX and the temperature  $T$  to set the continuum level of the flux. While this is an important subject to address for exoplanets with richer chemistry and an interest in the correct retrieval of varying abundances, we fixed the abundance to a constant value, which is a common approach in modelling hot-Jupiter atmospheres (Lecavelier Des Etangs et al. 2008; Agúndez et al. 2014; Steinrueck et al. 2019). Nonetheless, the effect of varying the sodium abundance on the results is discussed qualitatively in Sect. 4. With respect to the temperature, we explored a deviation from an isothermal treatment of the atmosphere by introducing a temperature gradient to verify if the common assumption of an isothermal atmosphere can also be applied here. Lastly, Seidel et al. (2020b) reported that MERC retrieved the best-fit parameters in two stages, first on the continuum, far from the line doublet, to obtain the appropriate range of possible parameters for NaX and  $T$ , and then on the line to further constrain the continuum parameters and the wind speeds and directions. The update to the code presented here includes additional parallelisation and now allows selecting a slightly wider wavelength range of three times the full width at half maximum (FWHM), thus combining the line core with enough of the continuum to eliminate the need for a two-tier retrieval as used by Seidel et al. (2020b). Further details on degeneracies, line broadening types, and the continuum parameter can be found in the first paper on MERC Seidel et al. (2020b), and in the works on which the forward model is based (Ehrenreich et al. 2006; Pino et al. 2018).

## 4. Retrieval results

We applied MERC with its updates presented in Sect. 3 to the combined HARPS and ESPRESSO dataset presented in Sect. 2. We examined multiple forward models, all with added planetary rotation: an isothermal temperature profile (iso), a temperature gradient ( $T$  grad), both with no added winds, and an isothermal

temperature profile combined with various wind patterns: a uniform day to nightside wind (called dtn in the following tables and figures), a  $\cos\theta$  dependent day- to nightside wind (dtn<sub>cos $\theta$</sub> ), a uniform super-rotational wind (srot), a  $\cos\theta$  dependent super-rotational wind (srot<sub>cos $\theta$</sub> ), a vertical wind (ver), and lastly, a two-layer approach with either a super-rotational or day- to night-side wind in the lower atmosphere combined with a vertical wind in the upper atmosphere. The switch between atmospheric layers was tested at different pressures (dtn<sub>cos $\theta$</sub> , ver; dtn, ver; srot, ver).

One of the most prominent features of Bayesian retrieval is the application of priors. Priors set the boundary conditions for the parameter space and allow adding knowledge of the physical properties to the numerical analysis of the fits. The priors used in this work are listed in Table 4. The priors for the mean isothermal temperature  $T_{\text{iso}}$  and the degenerate continuum parameter NaX were set to exclude non-physical results in terms of temperature, pressure, and sodium abundance. The velocity parameters were set more freely, from the lowest value close to zero to velocity ranges far beyond the escape velocity. The velocity priors were set each in both directions and had no sign. The effect of the priors is discussed in Sect. 4. The plotting range of the posteriors in Appendix A was selected for visibility and does not reflect the entire prior range.

The isothermal model without added winds (but taking planetary rotation into account) is the simplest model and served as our base to calculate the significance of the Bayesian evidence for all other models with  $|\ln \mathcal{Z}| = 2111.55 \pm 0.29$ . The Bayesian evidence of each model, as well as the significance of the model according to the Jeffrey scale in Table 3, is shown in Table 5 with a visual representation of the strength of evidence in Fig. 4. The posteriors from the nested-sampling retrieval as corner plots are shown in Appendix A, with the mean values at the top of each column and the parameters retrieved with the highest Bayesian evidence marked in blue.

### 4.1. Temperature profiles

Comparing the Bayesian evidence of the temperature gradient model to the isothermal model shows that there is not sufficient evidence for one model over the other. The temperature gradient was approximated through a base and a top temperature, where the base is the continuum level of the data and the top the highest probed layer of the atmosphere. The temperature-gradient model converges towards the isothermal solution and is then punished for the additional parameter with lower Bayesian

**Table 5.** Comparison of the different models.

Model	$ \ln Z $	$ \ln \mathcal{B}_{01} $	Strength of evidence <sup>(a)</sup>
Isothermal	$2111.55 \pm 0.29$	–	–
$T$ gradient	$2110.72 \pm 0.30$	–0.83	No evidence
dt <sub>n</sub>	$2114.23 \pm 0.39$	2.68	Moderate evidence
dt <sub>n,cos<math>\theta</math></sub>	$2112.46 \pm 0.35$	0.91	No evidence
srot	$2116.00 \pm 0.38$	4.45	Moderate evidence
srot <sub>cos<math>\theta</math></sub>	$2115.87 \pm 0.37$	4.32	Moderate evidence
ver	$2124.07 \pm 0.34$	12.52	Strong evidence
srot, ver	$2122.86 \pm 0.36$	11.31	Strong evidence
<b>dt<sub>n</sub>, ver</b>	$2125.17 \pm 0.39$	13.62	Strong evidence
dt <sub>n,cos<math>\theta</math></sub> , ver	$2123.82 \pm 0.32$	12.27	Strong evidence

**Notes.** <sup>(a)</sup>The base model to calculate  $|\ln \mathcal{B}_{01}|$  is the isothermal model without added wind patterns. The comparison stems from the Jeffrey scale in Table 3. The model with the highest Bayesian evidence is highlighted in bold.

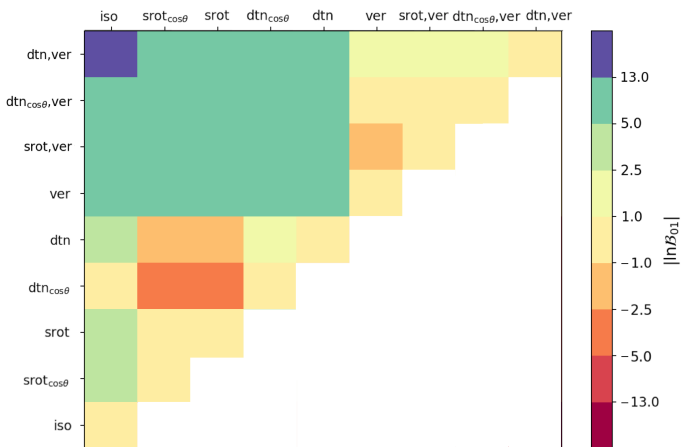


**Fig. 4.** Visualisation of the difference in Bayesian evidence of Table 5. The colour scale indicates  $|\ln \mathcal{B}_{01}|$  with the colours set at the different limits of the Jeffrey scale (Table 3), with strong evidence in green and the overall highest evidence in purple. The temperature gradient model is left out of the visualisation because it has a lower Bayesian evidence than even the base model. The model with the highest evidence (uniform day- to nightside wind in the lower and vertical wind in the upper atmosphere) shows strong evidence compared with all rotational models and moderate evidence with the vertical model and all two-layer models, see top row. For the exact values, see Table 5.

evidence (see Fig. A.2). We therefore used an isothermal temperature profile throughout all other retrieved models, which should only be interpreted as an upper limit mean temperature in light of the variation of the datasets in line depths and the intrinsic nature of transit observations as a mean over the terminator. The application of a homogeneous mean temperature profile, however, does not rule out the existence of a temperature gradient that might be temporally variable and averaged over in the combined dataset. The combined dataset is needed to properly constrain winds in the atmosphere, the main goal of this work. A more in-depth treatment of temporal temperature variations in the atmosphere of WASP-76 b is deferred to future work. The range of retrieved temperatures for all models is higher than the equilibrium temperature of WASP-76 b. The approximate temperature of 3300–3400 K for the hottest part in the higher layers of the atmosphere retrieved for the models presented here

is even higher than expected from Ehrenreich et al. (2020). The temperature retrieval is driven by the line depth and thus affected by the level of the continuum and the accuracy of the line depth and system parameters. In MERC, we take Rayleigh scattering into account, but do not account for the effects of H<sup>-</sup> opacity (Gandhi et al. 2020) on the continuum level for computational reasons. Therefore the temperature should be interpreted as an upper boundary only. However, even as an upper limit, the temperature remains curiously high, and the effect and likely cause are discussed in Sect. 5.

#### 4.2. Latitude-dependent wind patterns

Of all models presented in this section, only those with a day- to nightside wind or a super-rotational wind could show a latitude dependence. In most studies using GCMs, these wind patterns are restricted to bands along the equator (called jets) and weaken towards the poles (Showman et al. 2009, 2018; Parmentier et al. 2018). We approximated this behaviour by introducing a solid-body rotation dependence ( $\cos \theta$ ) to the wind pattern, as described in Sect. 3.1. The wind speeds retrieved for all models in this section ( $2\text{--}4 \text{ km s}^{-1}$ ) are compatible with GCM studies (e.g. Showman et al. 2018; Parmentier et al. 2018). Comparing the Bayesian evidence between the uniform wind patterns and their  $\cos \theta$  counterparts shows no evidence for a better fit with a jet-like structure for super-rotational wind ( $|\ln \mathcal{B}_{01}| = 0.13$ ), weak evidence for a better fit with a uniform wind pattern for the day- to nightside wind over a jet-like structure ( $|\ln \mathcal{B}_{01}| = 1.77$ ), and weak evidence for a better fit when the uniform wind pattern is applied to the lower atmosphere ( $|\ln \mathcal{B}_{01}| = 1.36$ ) in the combined wind patterns (lower day- to nightside wind and upper vertical wind). Although the evidence for a preference of the uniform wind patterns with no latitude dependence is only weak (see Table 3), it shows that for WASP-76 b, the winds are likely not primarily restricted in jets and flow more evenly across the terminator. However, this does not rule out any jet-like structure in the lower atmosphere of WASP-76 b, especially a multi-jet scenario as seen for Jupiter (Liu & Schneider 2010) that would look identical to a wide jet when integrated over the atmosphere.

#### 4.3. Uniform wind patterns

All tested uniform wind patterns show moderate to strong evidence for a better fit when compared to the base model without winds (see Table 5). A vertical wind throughout the atmosphere at  $30.8^{+3.1}_{-3.1} \text{ km s}^{-1}$  is not only preferred over the base model ( $|\ln \mathcal{B}_{01}| = 12.52$ , strong evidence), but also over the next-best wind pattern ( $|\ln \mathcal{B}_{01}| = 8.07$ , strong evidence). This indicates that a strong vertical wind is needed to create the broadened line shape, which cannot be created solely from a moderate day- to nightside or super-rotational wind at the retrieved velocities of  $2\text{--}4 \text{ km s}^{-1}$ .

Comparing the day- to nightside wind with the super-rotational wind, it appears at first glance that the super-rotational wind is preferred ( $|\ln \mathcal{B}_{01}| = 1.77$ , weak evidence). This serves as an excellent reminder to be aware of model limitations and blind application of nested sampling. The super-rotational broadening splits the sodium doublet into two sub-peaks, one that is redshifted at the morning terminator, and another that is blueshifted at the evening terminator, which creates a strong broadening in the wings. Consequently, every part of the atmosphere receives some shift, and the line depth is severely decreased by a strong